Ground states of two-dimensional tilted dipolar bosons with density-induced hopping

Chao Zhang,[1,2,*,†] Jin Zhang,[3,*,‡] Jin Yang,[4] and Barbara Capogrosso-Sansone[5]
[1]*State Key Laboratory of Precision Spectroscopy, East China Normal University, Shanghai 200062, China*
[2]*Department of Physics, University of Massachusetts, Amherst, Massachusetts 01003, USA*
[3]*Department of Physics and Astronomy, University of Iowa, Iowa City, Iowa 52242, USA*
[4]*Department of Physics, University of Virginia, Charlottesville, Virginia 22904, USA*
[5]*Department of Physics, Clark University, Worcester, Massachusetts 01610, USA*

(Received 15 December 2020; revised 24 March 2021; accepted 15 April 2021; published 29 April 2021)

Motivated by recent experiments with ultracold magnetic atoms trapped in optical lattices where the orientation of atomic dipoles can be fully controlled by external fields, we study, by means of quantum Monte Carlo, the ground-state properties of dipolar bosons trapped in a two-dimensional lattice with density-induced hopping and where the dipoles are tilted along the xz plane. We present ground-state phase diagrams of the above system at different tilt angles. We find that as the dipolar interaction increases, the superfluid phase at half-filling factor is destroyed in favor of either a checkerboard or stripe solid phase for tilt angle $\theta \lesssim 30^\circ$ or $\theta \gtrsim 30^\circ$, respectively. More interesting physics happens at tilt angles $\theta \gtrsim 58^\circ$, where we find that as the dipolar interaction strength increases, solid phases first appear at filling factor lower than 0.5. Moreover, unlike what is observed at lower tilt angles, we find that at half filling, a stripe supersolid intervenes between the superfluid and stripe solid phase.

DOI: 10.1103/PhysRevA.103.043333

I. INTRODUCTION

Long-range interactions have attracted a great deal of attention in the cold atom community, as they have been theoretically shown to stabilize a plethora of exotic quantum phases [1]. State-of-the-art ultracold experiments have paved the way to experimentally explore these exotic phases. Long-range interactions can be realized with ultracold atoms with large magnetic moments [2–4], by Rydberg dressing atoms [5,6], or with ultracold dipolar molecules [7–12]. The latter can realize strong dipolar long-range interactions, which may demand an extension or a revision of the standard Bose-Hubbard model [13–16]. Another way to realize long-range interactions is implementing an optical lattice in an optical cavity where the long-range interaction is mediated by strong matter-light interaction inside the cavity [17,18]. This possibility has triggered extensive theoretical endeavors into long-range interaction mediated by optical cavities [19–25]. Other theoretical notable works focused on long-range interactions in the presence of disorder or doping [26,27], which can be easily implemented in ultracold experiments. Since optical lattices are remarkably versatile compared to solid-state experiments, there have been several pioneering theoretical works considering long-range interactions in optical lattices with anisotropic tunneling rates [28,29]. These works so far are limited to multiple layers of one-dimensional optical lattices due to the large computational resources needed with the increase of the number of nearest neighbors in three dimensions. In ultracold experiments, both strengths and directions of magnetic or electric field can be freely tuned. As a result, the direction of dipoles can be adjusted freely. In recent years, many efforts have been directed toward exploring the physics of long-range dipolar interactions with different tilt angles [30–38].

Dipolar interactions are anisotropic. When two dipoles are placed side by side, they repel each other; when they are placed head to tail, they attract each other. Most of the early studies on dipolar interactions focused on systems with dipoles aligned perpendicular or parallel to the lattice plane. Tilted dipolar interactions with arbitrary angles have been theoretically studied in ultracold gases systems without lattice potentials (and are thus not based on Hubbard model) [35–40], or in lattices using renormalization group [34], mean-field theory [30,31], and variational approaches [1]. In Ref. [33], the authors used the quantum Monte Carlo method and found the ground-state phase diagram as a function of tilt angle θ at half filling and for hard-core bosons. For soft-core bosons, the ground-state phase diagrams have been found for tilt angles in the range $0 \leqslant \theta \leqslant 45^\circ$ [32]. The above-mentioned studies do not consider density-induced hopping, and, more generally, the details of how the parameters tuned experimentally, i.e., the scattering length, the dipole moment, and the depth of the optical lattice potential affect the on-site interaction, the long-range interaction, and the hopping strength entering the effective model used to describe the system. A recent experiment [2] has realized dipolar bosons in a three-dimensional lattice and considered how all the experimentally tunable parameters, such as scattering length and dipolar interaction strength, affect on-site and long-range interaction and hopping. This experiment paves the way to investigate quantum phase transitions of tilted dipolar lattice bosons with density-induced hopping.

*These authors contributed equally to this paper.
†chaozhang@umass.edu
‡jin-zhang@uiowa.edu

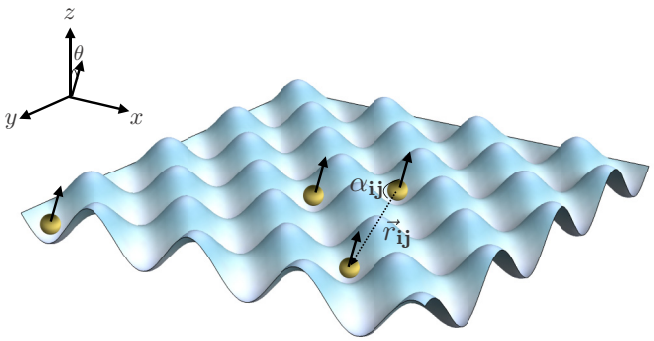

FIG. 1. Schematic representation of the system. Dipoles are trapped in a two-dimensional optical lattice and are aligned parallel to each other along the direction of polarization, determined by an electric/magnetic field. θ is the angle between polarization and z direction, $\vec{r}_{\mathbf{ij}}$ is the relative position between site $\mathbf{i}$ and $\mathbf{j}$. $\alpha_{\mathbf{ij}}$ is the angle between polarization and $\vec{r}_{\mathbf{ij}}$.

In this paper we use path-integral Monte Carlo simulations based on the worm algorithm [41] to study the ground-state phase diagram of dipolar bosons in a two-dimensional lattice with density-induced hopping where the dipoles are tilted on the xz plane. In the absence of a sign problem, the path-integral Monte Carlo method in continuous time is approximation-free and produces unbiased results, that is, errors are controllable and purely statistical. We calculate the parameters entering the effective model, i.e., the on-site interaction, long-range interaction strength, and density-induced hopping, from the parameters that can be tuned experimentally, such as the scattering length, dipolar interaction strength, and optical lattice potential depth. The paper is organized as follows: In Sec. II we introduce the Hamiltonian of the system and the parameters that can be controlled in experiments. In Sec. III we discuss various phases and the corresponding order parameters. In Sec. IV we present the phase diagrams of the above system at four tilt angles and discuss the nature of the transitions. In Sec. V we briefly discuss the experimental realization. We conclude the article in Sec. VI.

II. HAMILTONIAN

We study dipolar bosons with atomic mass m in a square optical lattice created by a separable external potential $V_{\text{ext.}}(x,y,z) = V_0[\cos^2(k_L x) + \cos^2(k_L y)] + m\Omega_z^2 z^2/2$. The laser beams with a wavelength $\lambda = 2a$ (a the lattice spacing) in the xy plane generate a two-dimensional square lattice with $k_L = 2\pi/\lambda$ the lattice momentum. The lattice depth is written in units of recoil energy $V_0 = sE_R$. The recoil energy $E_R = \hbar^2 k_L^2/2m$ defines a natural energy scale of the system. Ω_z is the frequency of the harmonic trap in the z direction, controlling the thickness of the two-dimensional sheet, from which we define the lattice flattening constant $\kappa = \hbar\Omega_z/2E_R$ [14]. As shown in Fig. 1, we assume all dipole moments to be in the same direction and to rotate in the xz plane with tilt angle θ between the dipole moment and the z axis. The many-body Hamiltonian describing this system in the second quantization language reads

$$\hat{H} = \int d^3\mathbf{r}\psi^\dagger(\mathbf{r})\left[-\frac{\hbar^2\nabla^2}{2m} + V_{\text{ext.}}(\mathbf{r})\right]\psi(\mathbf{r}) + \frac{1}{2}\int \psi^\dagger(\mathbf{r})\psi^\dagger(\mathbf{r}')V(\mathbf{r}'-\mathbf{r})\psi(\mathbf{r}')\psi(\mathbf{r})d^3\mathbf{r}d^3\mathbf{r}', \quad (1)$$

where $\psi^\dagger$ (ψ) is the bosonic creation (annihilation) field operator. The interaction between dipolar bosons contains contact (V_c) and dipole-dipole (V_{dd}) interactions,

$$V(\mathbf{r}-\mathbf{r}') = V_c(\mathbf{r}-\mathbf{r}') + V_{dd}(\mathbf{r}-\mathbf{r}') = \tilde{g}\delta(\mathbf{r}-\mathbf{r}') + \tilde{\gamma}\frac{1-3\cos^2(\alpha)}{|\mathbf{r}-\mathbf{r}'|^3}, \quad (2)$$

with $\tilde{g} = 4\pi\hbar^2 a_s/m$, a_s the s-wave scattering length, and $\tilde{\gamma} = \mu_e^2/(4\pi\epsilon_0)$ or $\mu_0\mu_m^2/4\pi$, μ_e (μ_m) the electric (magnetic) dipole moment of bosons, and ϵ_0 (μ_0) the vacuum permittivity (permeability). α is the angle between the direction of dipole moments and the relative position of two bosons. The bosonic field operator can be expanded with Wannier functions [42] in the lowest Bloch band $\psi(\mathbf{r}) = \sum_{\mathbf{i}} W_{\mathbf{i}}(x,y,z)\hat{a}_{\mathbf{i}}$. One then arrives at the extended Bose-Hubbard (EBH) model:

$$H = -t\sum_{\langle\mathbf{i},\mathbf{j}\rangle} a_{\mathbf{i}}^\dagger a_{\mathbf{j}} + \frac{U}{2}\sum_{\mathbf{i}} n_{\mathbf{i}}(n_{\mathbf{i}}-1) + \frac{1}{2}\sum_{\mathbf{i},\mathbf{j}} V_{\mathbf{i},\mathbf{j}} n_{\mathbf{i}} n_{\mathbf{j}} - \sum_{\langle\mathbf{i},\mathbf{j}\rangle} T_{\mathbf{i},\mathbf{j}} a_{\mathbf{i}}^\dagger (n_{\mathbf{i}} + n_{\mathbf{j}}) a_{\mathbf{j}} - \mu\sum_{\mathbf{i}} n_{\mathbf{i}}, \quad (3)$$

where the first term is the kinetic energy characterized by the hopping amplitude t. Here $\langle\cdots\rangle$ denotes nearest-neighboring sites, and $a_{\mathbf{i}}^\dagger$ ($a_{\mathbf{i}}$) are bosonic creation (annihilation) operators satisfying the bosonic commutation relations $[a_{\mathbf{i}}, a_{\mathbf{j}}^\dagger] = \delta_{\mathbf{ij}}$. U is the on-site repulsive interaction, and $n_{\mathbf{i}} = a_{\mathbf{i}}^\dagger a_{\mathbf{i}}$ is the particle number operator. $V_{\mathbf{ij}}$ is the off-site interaction between sites $\mathbf{i}$ and $\mathbf{j}$. If the lattice is deep enough, $V_{\mathbf{ij}} \approx V[1-3\cos^2(\alpha)]/|\mathbf{i}-\mathbf{j}|^3$ (V is the nearest-neighbor interaction when dipole moments are along z axis), which is widely used in the EBH model to study phase transitions. For a perfect two-dimensional system, $\cos(\alpha) = \sin(\theta)\cos(\phi)$ with ϕ the polar angle of the relative position $\mathbf{i}-\mathbf{j}$ in the xy plane, the off-site dipole-dipole interactions in $\hat{\mathbf{x}}$ and $\hat{\mathbf{x}}+\hat{\mathbf{y}}$ directions are negative for $\theta > \sin^{-1}(1/\sqrt{3}) \approx 35.3^\circ$ and $\theta > \sin^{-1}(\sqrt{2/3}) \approx 54.7^\circ$, respectively, while those in y direction are positive and independent of θ because $\alpha = 90^\circ$. It can be shown that the contribution U^{dd} from the dipolar interaction to the on-site strength of the EBH model (see below) is zero at angle 54.7° because of the rotational symmetry of Wannier functions. T is the density-induced tunneling. We also introduce the chemical potential in the last term to control the total number of bosons. We neglect the pair tunneling term because its strength is very small (see Appendix).

All interaction parameters entering the Hamiltonian in Eq. (3) can be found from Eq. (1) by calculating integrals involving Wannier functions (see Appendix) in units of recoil energy and lattice coordinate $\mathbf{r} \to \mathbf{r}/a$, where $g = 8a_s/(\pi a)$, $\gamma = m\mu_e^2/(2\pi^3\epsilon_0\hbar^2 a)$ or $\mu_0\mu_m^2 m/(2\pi^3\hbar^2 a)$. Contact interactions and dipolar interactions in Eq. (1) give us two sets of parameters, U^c, $V_{\mathbf{i},\mathbf{j}}^c$, $T_{\mathbf{i},\mathbf{j}}^c$ and U^{dd}, $V_{\mathbf{i},\mathbf{j}}^{dd}$, $T_{\mathbf{i},\mathbf{j}}^{dd}$, that determine the Hamiltonian parameters $U = U^c + U^{dd}$,

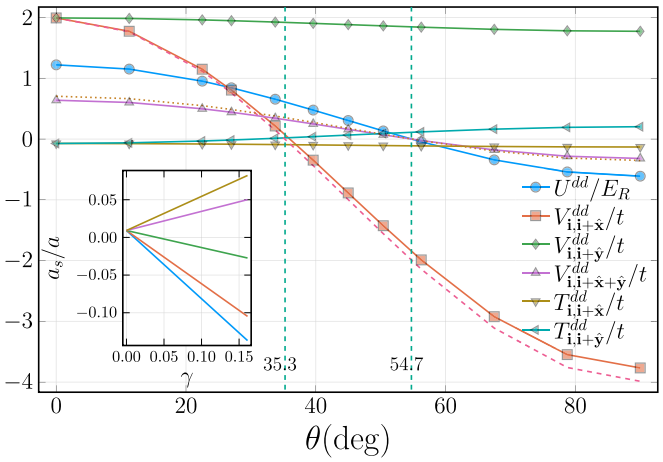

FIG. 2. Dipolar contribution to Hamiltonian parameters as a function of tilt angle θ at $\gamma = 1/\pi^3$, $s = \kappa = 10$. The two vertical dashed lines locate angles 35.3° and 54.7°, respectively. The dashed line by $V^{dd}_{\mathbf{i},\mathbf{i}+\hat{\mathbf{x}}}/t$ is $V(1-3\sin^2(\theta))$. The dotted line by $V^{dd}_{\mathbf{i},\mathbf{i}+\hat{\mathbf{x}}+\hat{\mathbf{y}}}/t$ is $V(1-3\sin^2(\theta)\cos^2(45°))/(\sqrt{2})^3$. Lines in the inset show a_s/a vs γ at fixed on-site interaction $U/t = 20$ for $\theta = 0°, 22.5°, 45°, 67.5°, 90°$ from bottom up, where $0 < \gamma < 0.16$ and $-0.137 < a_s/a < 0.082$.

$V = V^c + V^{dd}$, $T = T^c - T^{dd}$ [43]. We consider lattice depth $s = 10$ so that the tight-binding approximation for contact interactions holds. To obtain a valid approximation of a two-dimensional system, we need $\kappa \gg \sqrt{s}$ so that the energy gap in the z direction is much larger than the one in the xy plane. We use lattice flattening $\kappa = 10$. Then the tunneling $t = 0.0192E_R$ is fixed, where E_R is the recoil energy, while the parameters obtained from contact interactions (U^c, $V^c_{\mathbf{i},\mathbf{j}}$, $T^c_{\mathbf{i},\mathbf{j}}$) are proportional to g and those obtained from dipolar interactions(U^{dd}, $V^{dd}_{\mathbf{i},\mathbf{j}}$, $T^{dd}_{\mathbf{i},\mathbf{j}}$) are proportional to γ. We calculate off-site interactions $V^{dd}_{\mathbf{i},\mathbf{j}}$ for relative lattice positions $|\mathbf{i}-\mathbf{j}| \leqslant 5$ to keep track of long-range effects of dipolar interactions, while we only keep nearest-neighbor terms for hopping t and density-induced hopping T, since the decay of hopping and density-induced hopping is exponentially fast and the long-range part can be neglected.

In Fig. 2 we show how the parameters obtained from the dipolar interaction depend on the tilt angle θ for $\gamma = 1/\pi^3$. Notice that the dipolar part of on-site interaction U^{dd} is in units of recoil energy. As we increase the tilt angle, U^{dd}, the nearest-neighbor interaction in $\hat{\mathbf{x}}$ direction, $V^{dd}_{\mathbf{i},\mathbf{i}+\hat{\mathbf{x}}}$, and the next-nearest-neighbor interaction in $\hat{\mathbf{x}}+\hat{\mathbf{y}}$ direction $V^{dd}_{\mathbf{i},\mathbf{i}+\hat{\mathbf{x}}+\hat{\mathbf{y}}}$ go from positive to negative; $T^{dd}_{\mathbf{i},\mathbf{i}+\hat{\mathbf{y}}}/t$ goes from -0.073 to 0.203; $T^{dd}_{\mathbf{i},\mathbf{i}+\hat{\mathbf{x}}}/t$ is always negative from -0.073 to -0.131; and $V^{dd}_{\mathbf{i},\mathbf{i}+\hat{\mathbf{y}}}/t$ does not change much as expected. $V^{dd}_{\mathbf{i},\mathbf{i}+\hat{\mathbf{x}}} = 0$ at $\theta \gtrsim 35.3°$, and $U^{dd} = V^{dd}_{\mathbf{i},\mathbf{i}+\hat{\mathbf{x}}+\hat{\mathbf{y}}} = 0$ at angle 54.7°. The widely used approximation $V_{\mathbf{i},\mathbf{j}} \approx V[1-3\cos^2(\alpha)]/|\mathbf{i}-\mathbf{j}|^3$ is also plotted for $V^{dd}_{\mathbf{i},\mathbf{i}+\hat{\mathbf{x}}}$ (dashed line) and $V^{dd}_{\mathbf{i},\mathbf{i}+\hat{\mathbf{x}}+\hat{\mathbf{y}}}$ (dotted line) ($V^{dd}_{\mathbf{i},\mathbf{i}+\hat{\mathbf{y}}}$ in the approximation is a constant). We see that for $V^{dd}_{\mathbf{i},\mathbf{i}+\hat{\mathbf{x}}}$ and $V^{dd}_{\mathbf{i},\mathbf{i}+\hat{\mathbf{y}}}$, the approximation slightly deviates from the numerical results only at large angles, while it is good at all angles for $V^{dd}_{\mathbf{i},\mathbf{i}+\hat{\mathbf{x}}+\hat{\mathbf{y}}}$. The agreement between calculated parameters and the approximation indicates that the 2D approximation is valid. In the following we fix the on-site interaction $U/t = (U^c + U^{dd})/t = 20$ and study phase diagrams in the γ-n plane for different tilt angles θ, where n is the filling factor. The inset of Fig. 2 shows the dependence of a_s/a on γ with fixed $U/t = 20$. The largest γ we use to calculate the phase diagram is 0.16, and the s-wave scattering length in units of lattice spacing goes from -0.137 to 0.082 as we increase the tilt angle from 0° to 90°.

TABLE I. Quantum phases and the corresponding order parameters: superfluid density ρ_s, structure factor $S(\pi,\pi)$, and $S(0,\pi)$.

Phase	ρ_s	$S(\pi,\pi)$	$S(0,\pi)$
Superfluid (SF)	$\neq 0$	0	0
Checkerboard solid (CB)	0	$\neq 0$	0
CB Supersolid (CBSS)	$\neq 0$	$\neq 0$	0
Stripe Soild (SS)	0	0	$\neq 0$
Stripe Supersolid (SSS)	$\neq 0$	0	$\neq 0$

III. QUANTUM PHASES AND ORDER PARAMETERS

In this section we list the phases stabilized by Eq. (3) and the corresponding order parameters. Table I shows order parameters for the superfluid (SF) phase, checkerboard solid (CB) phase, checkerboard supersolid (CBSS) phase, stripe solid (SS) phase, and stripe supersolid (SSS) phase. Each phase corresponds to a unique combination of the order parameters. Here, three order parameters are needed in order to characterize the quantum phases: superfluid density ρ_s, structure factor $S(\pi,\pi)$, and $S(0,\pi)$.

The superfluid density is calculated in terms of the winding number [44]: $\rho_s = \langle \mathbf{W}^2 \rangle / dL^{D-2}\beta$, where $\mathbf{W}$ is the winding number and $\mathbf{W}^2 = W_x^2 + W_y^2$. The structure factor characterizes diagonal long-range order and is defined as $S(\mathbf{k}) = \sum_{\mathbf{r},\mathbf{r}'} \exp[i\mathbf{k}\cdot(\mathbf{r}-\mathbf{r}')]\langle n_{\mathbf{r}} n_{\mathbf{r}'}\rangle/N$, where N is the particle number. Here, $\mathbf{k}$ is the reciprocal lattice vector. We use $\mathbf{k} = (\pi,\pi)$ and $\mathbf{k} = (0,\pi)$ to identify the CB and SS phases, respectively.

IV. GROUND-STATE PHASE DIAGRAMS

In this section we present ground-state phase diagrams of dipolar bosons in a square lattice and with density-induced hopping. The dipoles are parallel to each other and are tilted in the xz plane. Figure 3 shows the ground-state phase diagram for four tilt angles $\theta = 0°$, 11.25°, 45°, and 67.5° at fixed $U/t = 20$. The x axis is the filling factor $n = N/N_{\text{site}}$, where N is the particle number, and $N_{\text{site}} = L \times L$, with L the system size. The y axis is the dipolar interaction strength γ. The transition points on the phase diagrams are determined using system sizes $L = 20$, 40, and 60 and inverse temperature $\beta = L$. This choice assures that temperature is low enough so that we are effectively at zero temperature and we are therefore probing ground-state properties. For second-order phase transitions we have performed standard finite-size scaling.

In Fig. 3(a) we plot the phase diagram for the system with all dipoles tilted perpendicularly to the xy plane. If we

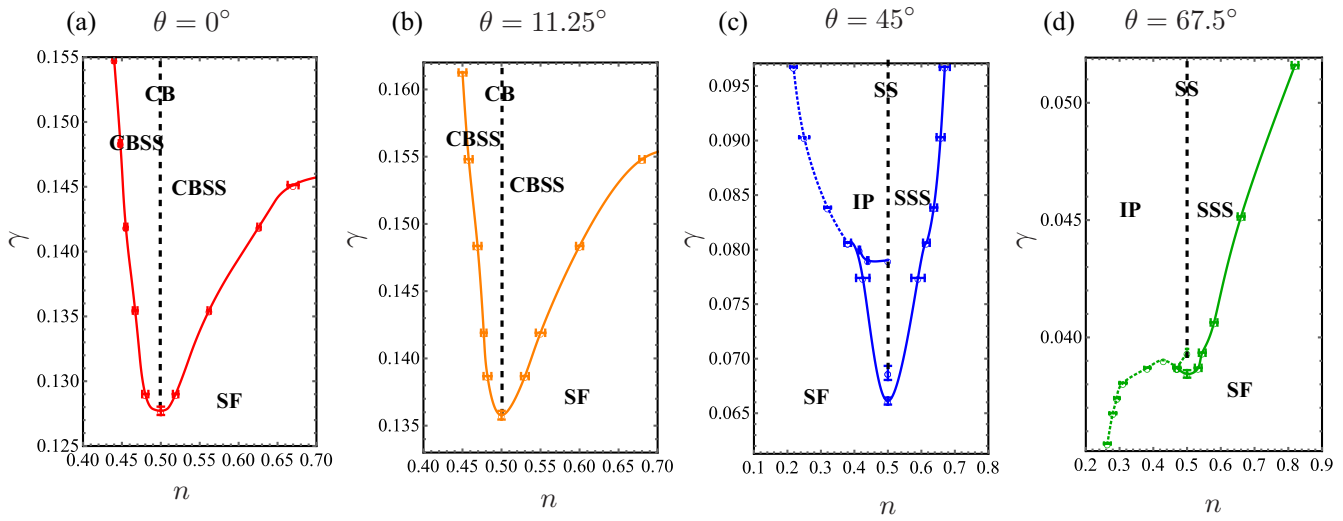

FIG. 3. Ground-state phase diagram for $\theta = 0°$(a), $\theta = 11.25°$(b), $\theta = 45°$(c), and $\theta = 67.5°$(d). The x axis is filling factor n and the y axis is the dipolar interaction strength γ. For tilt angles $\theta \lesssim 30°$, the solid phase stabilized at half filling corresponds to a checkerboard solid (CB) and the supersolid phase is a CBSS; for $\theta \gtrsim 30°$, the solid phase corresponds to a stripe solid (SS) and the supersolid phase is a SSS. IP stands for the incompressible ground states stabilized at rational filling factors. Dotted lines correspond to first-order phase transitions, while solid lines correspond to second-order transitions. Dashed lines at filling factor $n = 0.5$ represent solid phases CB or SS. When not visible, error bars are within symbol size.

compare with results in Ref. [27], where density-induced hopping is not taken into account, we see that density-induced hopping does not affect the shape of the phase diagram and only enhances the superfluid region. This is because, at $\theta = 0$, one has $T_x > 0$ and $T_y > 0$. In Ref. [27], the SF-to-CB phase transition at half-filling happens at around $V/t \sim 4.6$, while with density-induced hopping, this transition happens around $\gamma = 0.128$ (equivalent to $V/t \sim 7.89$), for which the density-induced hopping $T_x/t \sim 0.355$ and $T_y/t \sim 0.355$. We were not able to resolve the nature of the CB-SF phase transition at $n = 0.5$. We did not detect a supersolid phase and found no evidence of a first-order phase transition (we changed the interaction strength γ in increments of 0.5%). For $\gamma > 0.128$, upon doping with particles or holes from half-filling, we enter the CBSS phase. Here diagonal long-range order and off-diagonal long-range order coexist as shown from a finite superfluid density ρ_s and a finite structure factor $S(\pi, \pi)$. The CBSS phase is more robust on the particle side. For large enough doping, on both particle and hole sides the supersolid disappears in favor of a SF phase via a second-order phase transition.

In Fig. 3(b) we show the phase diagram at tilt angle $\theta = 11.25°$. The qualitative shape of the phase diagram is the same as in Fig. 3(a) but with a more extended SF region (note the difference in the range of y axis). Here, too, the density-induced hopping parameters are positive. At this angle the repulsive interaction along the x direction has decreased, while the repulsive interaction along the y direction does not change significantly. This leads to a larger superfluid region compared to the $\theta = 0°$ phase diagram. We investigated the SF-CB transition at filling factor $n = 0.5$ and found hysteresis curves as a function of the interaction strength γ for the superfluid density ρ_s and structure factor $S(\pi, \pi)$. These hysteresis curves signal a first-order phase transition.

There exists a qualitative change in the phase diagrams in going from $\theta = 11.25°$ to $\theta = 45°$. This change happens at $\theta \sim 30°$, where the solid phase and the supersolid phase change from the CB pattern to SS pattern. From Ref. [33], we know that there exists an emulsion phase at $\theta \sim 30°$ which is challenging to resolve numerically. Phase diagrams $\theta \lesssim 30°$ have a similar shape to the one at $\theta = 11.25°$, while phase diagrams for $30° \lesssim \theta \lesssim 58°$ have a similar shape to the one at $\theta = 45°$. For larger tilt angles, phase diagrams are similar to the one for $\theta = 67.5°$.

Figure 3(c) shows the ground-state phase diagram at tilt angle $\theta = 45°$. At this angle the density-induced hopping along the y direction, T_y, is negative while T_x is positive with $0.063 < |T_y|/t < 0.128$ and $0.27 < T_x/t < 0.373$ for the range of γ considered. The dipolar interaction along the x axis is attractive, stabilizing a stripe solid phase at filling factor $n = 0.5$ and $\gamma \gtrsim 0.068\,69$. Since $T_x > |T_y|$, compared to the case with no density-induced hopping for which we find that the SS phase at half filling appears at $\gamma \sim 0.0564$, we observe an enhanced SF region. We have studied the transition from SF to SS at half filling and observed that a supersolid intervenes in between within a narrow range, $0.066\,11 < \gamma < 0.068\,69$. For $0.068\,69 < \gamma < 0.0790$, a SSS phase also appears upon doping the stripe solid with particles or holes. Interestingly, as γ further increases only the SSS phase on the particle side survives (for low enough doping), while on the hole side the SSS phase disappears in favor of a succession of incompressible ground states stabilized at rational filling factors (this succession will become dense in the thermodynamic limit), similar to the classical devil's staircase [45–47]. This is seen in Fig. 4, where filling factor n is plotted as a function of chemical potential μ/U at $L = 40$, $\theta = 45°$, $U/t = 20$, and $\gamma = 0.0967$. When $\mu/U > -0.12$, one can observe several plateaus at different rational filling factors. These plateaus correspond to incompressible ground

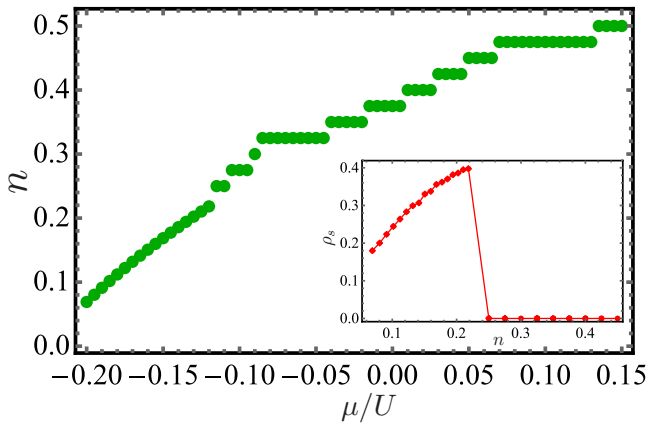

FIG. 4. Plots correspond to parameters $U/t = 20$, $\theta = 45°$, $\gamma = 0.0967$, and $L = 40$. Main plot: filling factor n as a function of μ/U. Inset: superfluid density ρ_s as a function of filling factor n. When not visible error bars are within symbol size.

states. For all filling factors considered, we have observed a stripe phase similar to the one at $n = 0.5$, the only difference being that the spacing between stripes changes with filling factor and can be irregular to accommodate a certain filling. The inset shows the superfluid density ρ_s as a function of filling factor n. At lower filling factor, the SF density is finite but goes to zero abruptly at $n \sim 0.25$. This abrupt change in ρ_s indicates that the SF phase disappears in favor of the incompressible phase through a first-order phase transition, as confirmed from hysteretic behavior in the n vs μ/U curve (not shown here). Finally, we notice that we did not find any staggered SF, expected for larger $|T_y|$ and/or larger filling factor [48].

The shape of the ground-state phase diagram changes on the hole side when $\theta \gtrsim 58°$. Figure 3(d) shows the phase diagram at tilt angle $\theta = 67.5°$. At this angle, the density-induced hopping along the y direction T_y is negative, while T_x is positive with $0.111 < |T_y|/t < 0.193$ and $0.202 < T_x/t < 0.264$ for the range of γ considered. Interestingly, we find incompressible ground states at lower filling factor which are stabilized for values of γ smaller than what is required to stabilize the stripe solid at half filling. This incompressible phase is realized at fractional filling factors, in analogy with what is discussed in regards to the incompressible phase observed at $\theta = 45°$. Evidence of this phase is shown in Fig 5(a), where we plot the filling factor n as a function of chemical potential μ/U at $L = 60$, $\theta = 67.5°$, $U/t = 20$, and $\gamma = 0.0387$. When $\mu/U < -0.202$, corresponding to $n < 0.38$, we observe density plateaus which terminate with an abrupt change of n from a finite value to zero. The plateaus correspond to the incompressible ground states realized at fractional filling factors, and the abrupt change indicates that the incompressible phase terminates via a first-order phase transition, as confirmed by hysteretic behavior in the n vs μ curve (not shown here). For $n \simeq 0.38$, the system enters the SF phase [note the reentrant shape of the phase diagram in Fig. 3(d)]. Superfluidity persists at $n = 0.5$, where a supersolid phase is observed. Correspondingly, there does not exist a plateau in the n vs μ curve at $n = 0.5$ (thus excluding the existence of an incompressible phase at half filling for this value of γ),

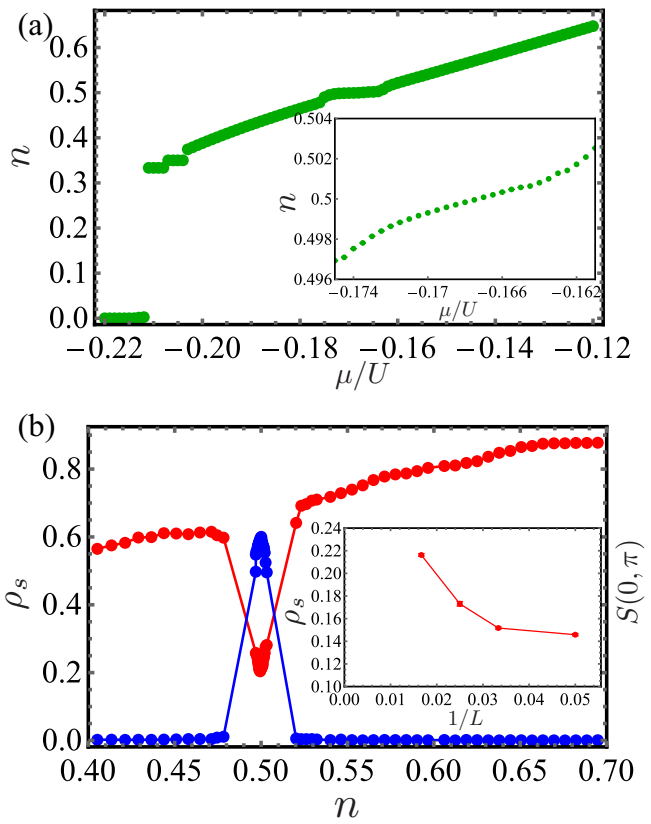

FIG. 5. Main plots correspond to parameters $U/t = 20$, $\theta = 67.5°$, $\gamma = 0.0387$, and $L = 60$. (a) Filling factor n as a function of μ/U. Inset shows the filling factor n as a function of μ/U around half filling. (b) Superfluid density ρ_s and structure factor $S(0, \pi)$ as a function of filling factor n. Inset shows the superfluid density ρ_s as a function of $1/L$ at filling factor $n = 0.5$. When not visible error bars are within symbol size.

as seen in the inset where we show a blowup of the main figure around filling factor $n = 0.5$. Indeed, at $n = 0.5$, we observe that a SSS phase intervenes between the SF and the SS phase. This supersolid phase exists in the range $0.0384 \lesssim \gamma \lesssim 0.0394$. Evidence of the supersolid at half filling is shown in Fig. 5(b), where we plot superfluid density ρ_s and structure factor $S(0, \pi)$ as a function of filling factor n at $L = 60$, $\theta = 67.5°$, $U/t = 20$, and $\gamma = 0.0387$. One can clearly see the coexistence of superfluidity and solid order at $n = 0.5$. Here a finite ρ_s persists (and increases) as the system size is increased, as shown in the inset of Fig. 5(b) where we plot the superfluid density as a function of $1/L$ at $n = 0.5$. Overall, since $T_x > |T_y|$, we observe an enhanced SF region compared to the case with no density-induced hopping, for which the SS at half filling appears at $\gamma \sim 0.0358$ and the transition from SF to IP is shifted downward by ∼5%. We notice that in the parameter region considered, we have not found any evidence of staggered SF.

V. EXPERIMENTAL REALIZATION

Various ultracold bosonic systems with different particle species are capable of exploring the phase diagrams proposed above. These systems include atoms with magnetic dipole

moments such as Cr [3,49], Er [2,50,51], and Dy [11,12], polar molecules such as Er_2 [9], KRb [7], NaK [10], and Rydberg dressing atoms [5,52]. The two-dimensional system can be realized by loading BEC ensembles into optical lattices formed by overlapping three perpendicularly crossed laser beams with their retroreflected beams. While the trap depths along two dimensions are equal, the trap depth along the third dimension should be much larger to keep the lattice system two-dimensional or quasi-two-dimensional. The orientation of the electric or magnetic dipole moments can be adjusted freely using external electric or magnetic fields, and the value of γ depends on lattice constant, external fields, gas species, and which states they are in. The filling factor n can be tuned by changing trap depth and on-site interactions through the Feshbach field. The Feshbach resonance also makes the a_s/a ratios proposed in this work all accessible. When the lattice constant equals 532 nm, for Cr which has a γ of $\sim$0.06, the superfluid phase should be observed when $\theta = 0^\circ, 11.25^\circ, 45^\circ$. When $\theta = 67.5^\circ$, the incompressible phase, SS phase, and SSS phase are realized under different filling conditions. For Er, Dy which have larger dipole moments (Er: $\gamma \sim 0.27$, Dy: $\gamma \sim 0.53$), different quantum phases other than the superfluid can be realized under different filling conditions at any tilt angle. If the lattice constant changes from 532 nm to 266 nm, the γ values above are changed by a factor of 2. When using ultracold polar molecules, even larger dipole moments, correspondingly γ, can be obtained. For example, the ultracold polar molecule Er_2 can give a γ as high as $\sim$6.20 and hence the entire phase diagram can be explored.

Various detection methods are capable to detect the phases arising under different conditions. The above-discussed systems with different tilt angles are in the SF phase when γ is small. The SF phase can be detected by observing interference patterns in the time-of-flight imaging of the ultracold quantum gases released from traps [53,54]. Several other quantum phases emerge after increasing γ. These phases pose challenges to time-of-flight detection. However, ultracold quantum gases in these phases have modulated density distributions in lattices, for example, SS and SSS have periodical density modulations in optical lattices, while CB has particles distributed with a checkerboard pattern in lattices. These patterns can be directly observed using state-of-the-art quantum gas microscopes with single-site-resolved imaging capacity [55–57]. The IP phase which has a modulated density distribution can also be feasibly observed using quantum gas microscopes.

VI. CONCLUSION

We have studied the ground states of soft-core dipolar bosons with density-induced hopping as described by the extended Bose-Hubbard model on a square lattice. Dipoles are tilted in the xz plane. The parameters entering the effective model are calculated starting from the parameters that can be tuned experimentally, e.g., scattering length and dipole moment, which both contribute to the on-site interaction, long-range interaction, and strength of density-induced hopping. We have found the ground-state phase diagrams of this system at tilt angles $\theta = 0^\circ$, 11.25°, 45°, and 67.5°. We have observed that as the dipolar interaction increases, the superfluid phase at half-filling factor is destroyed in favor of either a checkerboard or stripe solid phase for tilt angle $\theta \lesssim 30^\circ$ or $\theta \gtrsim 30^\circ$, respectively. At tilt angles $\theta \gtrsim 58^\circ$, we have found that as the dipolar interaction strength increases, solid phases first appear at filling factor lower than 0.5. For $\theta = 45^\circ$ and 67.5°, we have observed the presence of a supersolid phase intervenes between the superfluid and stripe solid phase at half filling. All the phases discussed here can be realized experimentally with magnetic atoms or polar molecules.

ACKNOWLEDGMENTS

We would like to thank Giovanna Morigi, Jacub Zakrzewski, Rebecca Kraus, and Peter Schauss for fruitful discussions. The computing for this project was performed at the OU Supercomputing Center for Education & Research (OSCER) at the University of Oklahoma (OU) and the cluster at Clark University.

APPENDIX: CALCULATION OF HAMILTONIAN PARAMETERS

In a separable lattice potential, the Wannier function can be written as $W(x, y, z) = w(x)w(y)w(z)$. $w(x)$ is the one-dimensional Wannier function in a one-dimensional optical lattice. In the lattice coordinates, $\mathbf{r} \to \mathbf{r}/a$, $w(z) = (\pi\kappa)^{1/4} \exp(-\pi^2\kappa z^2/2)$ is the ground-state wave function of the harmonic trap in z direction. The contribution to the parameters of the Bose-Hubbard model can be calculated separately for contact interaction and dipole-dipole interaction. Labeling the sites in the square lattice as $\mathbf{i} = (i_x, i_y)$, the general interaction comes from integrals of four Wannier functions at sites $\mathbf{i}, \mathbf{j}, \mathbf{k}, \mathbf{l}$. In units of the recoil energy, the contact interaction gives

$$U^c_{\mathbf{i},\mathbf{j},\mathbf{k},\mathbf{l}} = \frac{8a_s}{\pi a}\int d\mathbf{r} W^*_{\mathbf{i}}(\mathbf{r}) W^*_{\mathbf{j}}(\mathbf{r}) W_{\mathbf{k}}(\mathbf{r}) W_{\mathbf{l}}(\mathbf{r}) = \frac{8a_s}{\pi a}\sqrt{\frac{\kappa\pi}{2}}\int dxdy \mathcal{W}^*_{\mathbf{i}}\mathcal{W}^*_{\mathbf{j}}\mathcal{W}_{\mathbf{k}}\mathcal{W}_{\mathbf{l}}, \tag{A1}$$

where $\mathcal{W}_{\mathbf{i}} = w_{i_x}(x)w_{i_y}(y)$ is the two-dimensional Wannier function. Then the contribution to the Hamiltonian parameters from contact interaction are $U^c = U^c_{\mathbf{iiii}}$, $V^c_{ij} = U^c_{\mathbf{ijij}} + U^c_{\mathbf{ijji}} = 2U^c_{\mathbf{ijij}}$, $T^c_{\mathbf{ij}} = -(U^c_{\mathbf{iiij}} + U^c_{\mathbf{iiji}})/2 = -U^c_{\mathbf{iiij}}$, $P^c_{\mathbf{ij}} = U^c_{\mathbf{iijj}}$. Typical values of this contribution are $U^c/t = 30.5$, $V^c/t = 0.006$, $T^c/t = 0.104$, $P^c/t = 0.003$ for $a_s/a = 0.014$, corresponding to $a_s = 100a_0$ for ^{87}Rb at lattice spacing $a = 377$ nm [58,59].

The contributions from dipole-dipole interactions can be calculated by Fourier transform,

$$D_{\mathbf{i},\mathbf{j},\mathbf{k},\mathbf{l}} = \int d\mathbf{r}d\mathbf{r}' W^*_{\mathbf{i}}(\mathbf{r}) W^*_{\mathbf{j}}(\mathbf{r}') V_d(\mathbf{r}' - \mathbf{r}) W_{\mathbf{k}}(\mathbf{r}') W_{\mathbf{l}}(\mathbf{r}) = \frac{1}{(2\pi)^3}\int d\mathbf{k} \tilde{W}_{\mathbf{il}}(-\mathbf{k}) \tilde{V}_d(\mathbf{k}) \tilde{W}_{\mathbf{jk}}(\mathbf{k}), \tag{A2}$$

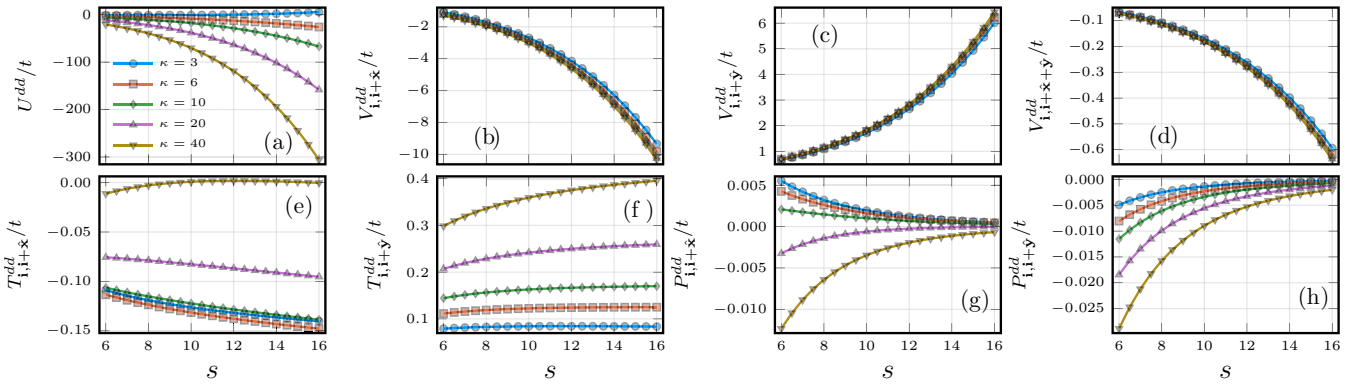

FIG. 6. Dipolar contribution to Hamiltonian parameters as a function of lattice depth s for $\kappa = 3, 6, 10, 20, 40$ at tilt angle $\theta = 67.5^\circ$ and $\gamma = 1/\pi^3$. We plot (a) on-site interaction U^{dd}/t; (b) nearest-neighbor interaction in $\hat{\mathbf{x}}$ direction $V^{dd}_{\mathbf{i},\mathbf{i}+\hat{\mathbf{x}}}/t$; (c) nearest-neighbor interaction in $\hat{\mathbf{y}}$ direction $V^{dd}_{\mathbf{i},\mathbf{i}+\hat{\mathbf{y}}}/t$; (d) next-nearest-neighbor interaction in $\hat{\mathbf{x}}+\hat{\mathbf{y}}$ direction $V^{dd}_{\mathbf{i},\mathbf{i}+\hat{\mathbf{x}}+\hat{\mathbf{y}}}/t$; (e) density-induced tunneling in $\hat{\mathbf{x}}$ direction $T^{dd}_{\mathbf{i},\mathbf{i}+\hat{\mathbf{x}}}/t$; (f) density-induced tunneling in $\hat{\mathbf{y}}$ direction $T^{dd}_{\mathbf{i},\mathbf{i}+\hat{\mathbf{y}}}/t$; (g) pair tunneling in $\hat{\mathbf{x}}$ direction $P^{dd}_{\mathbf{i},\mathbf{i}+\hat{\mathbf{x}}}/t$; and (h) pair tunneling in $\hat{\mathbf{y}}$ direction $P^{dd}_{\mathbf{i},\mathbf{i}+\hat{\mathbf{y}}}/t$.

where the Fourier transform of the product of two Wannier functions with the same coordinate $\mathbf{r}$ is

$$\tilde{W}_{\mathbf{il}}(\mathbf{k}) = \int d\mathbf{r} W^*_{\mathbf{i}}(\mathbf{r}) W_{\mathbf{l}}(\mathbf{r}) e^{-i\mathbf{k}\cdot\mathbf{r}} = e^{-\frac{k_z^2}{4\pi^2\kappa}} \int dx dy \mathcal{W}^*_{\mathbf{i}}(x,y) \mathcal{W}_{\mathbf{l}}(x,y) e^{-i(k_x x + k_y y)}. \tag{A3}$$

The Fourier transform of dipolar interaction reads

$$\tilde{V}_d(\mathbf{k}) = 4\pi\gamma\left(\cos^2(\beta) - \tfrac{1}{3}\right), \tag{A4}$$

where β is the angle between $\mathbf{k}$ and the dipole moment. We can further integrate out k_z,

$$D_{\mathbf{i},\mathbf{j},\mathbf{k},\mathbf{l}} = \frac{1}{(2\pi)^2} \int d\mathbf{k}_{xy} \tilde{\mathcal{W}}_{\mathbf{il}}(-\mathbf{k}_{xy}) \tilde{\mathcal{V}}(\mathbf{k}_{xy}) \tilde{\mathcal{W}}_{\mathbf{jk}}(\mathbf{k}_{xy}), \tag{A5}$$

and the effective two-dimensional interaction is

$$\tilde{\mathcal{V}}(\mathbf{k}_{xy}) = 2\pi\gamma \left\{ \sqrt{2\pi\kappa}\left(n_z^2 - \frac{1}{3}\right) + \left[\frac{(n_x k_x + n_y k_y)^2}{\sqrt{k_x^2 + k_y^2}} - n_z^2\sqrt{k_x^2 + k_y^2}\right] e^{\frac{k_x^2+k_y^2}{2\pi^2\kappa}} \operatorname{Erfc}\left[\sqrt{\frac{k_x^2 + k_y^2}{2\pi^2\kappa}}\right] \right\}, \tag{A6}$$

where $\mathbf{n} = (n_x, n_y, n_z)$ is the unit vector along the dipole moments, and $\operatorname{Erfc}(x)$ is the complementary error function. The dipolar part of Hamiltonian parameters are $U^{dd} = D_{\mathbf{iiii}}, V^{dd}_{\mathbf{ij}} = D_{\mathbf{ijij}} + D_{\mathbf{ijji}}, T^{dd}_{\mathbf{ij}} = D_{\mathbf{iiij}}, P^{dd}_{\mathbf{ij}} = D_{\mathbf{iijj}}$.

Some results for tilt angle $\theta = 67.5^\circ$ and $\gamma = 1/\pi^3$ are depicted in Fig. 6, where we show the dipolar contribution to Hamiltonian parameters as a function of lattice depth s for $\kappa = 3, 6, 10, 20, 40$. As the lattice depth s is increased, the dipolar contribution to on-site interaction increases from negative to positive for small $\kappa = 3$. For larger κ instead, it becomes more negative by increasing either s or κ. These behaviors are opposite to those at small tilt angles. The nearest-neighbor interaction in $\hat{\mathbf{x}}$ direction $V^{dd}_{\mathbf{i},\mathbf{i}+\hat{\mathbf{x}}}$ and the next-nearest-neighbor interaction in $\hat{\mathbf{x}}+\hat{\mathbf{y}}$ direction $V^{dd}_{\mathbf{i},\mathbf{i}+\hat{\mathbf{x}}+\hat{\mathbf{y}}}$ are negative as expected and become more negative by increasing either s or κ, while the nearest-neighbor interaction in $\hat{\mathbf{y}}$ direction $V^{dd}_{\mathbf{i},\mathbf{i}+\hat{\mathbf{y}}}$ behaves just the opposite. The dependence of off-site interactions on κ becomes negligible for large enough κ because we are approaching a perfect 2D lattice. The density-induced tunneling in $\hat{\mathbf{x}}$ direction is negative and becomes more negative by increasing s for $\kappa \leqslant 20$. If we increase κ with fixed s, it becomes more negative first but then increases and goes towards positive values. In the $\hat{\mathbf{y}}$ direction it becomes more positive by either increasing s or increasing κ. The dependence on s is very small for small κ. We notice that at small angles the density-induced tunneling goes from positive to negative as we increase κ. The pair tunneling is very small compared to other parameters, so we neglect it in the Hamiltonian.

[1] K. Góral, L. Santos, and M. Lewenstein, Phys. Rev. Lett. **88**, 170406 (2002).

[2] S. Baier, M. J. Mark, D. Petter, K. Aikawa, L. Chomaz, Z. Cai, M. Baranov, P. Zoller, and F. Ferlaino, Science **352**, 201 (2016).

[3] A. Griesmaier, J. Werner, S. Hensler, J. Stuhler, and T. Pfau, Phys. Rev. Lett. **94**, 160401 (2005).

[4] A. dePaz, A. Sharma, A. Chotia, E. Maréchal, J. H. Huckans, P. Pedri, L. Santos, O. Gorceix, L. Vernac, and B. Laburthe-Tolra, Phys. Rev. Lett. **111**, 185305 (2013).

[5] P. Schauß, J. Zeiher, T. Fukuhara, S. Hild, M. Cheneau, T. Macrì, T. Pohl, I. Bloch, and C. Gross, Science **347**, 1455 (2015).

[6] H. Bernien, S. Schwartz, A. Keesling, H. Levine, A. Omran, H. Pichler, S. Choi, A. S. Zibrov, M. Endres, M. Greiner, V. Vuletić, and M. D. Lukin, Nature (London) **551**, 579 (2017).

[7] B. Yan, S. A. Moses, B. Gadway, J. P. Covey, K. R. A. Hazzard, A. M. Rey, D. S. Jin, and J. Ye, Nature (London) **501**, 521 (2013).

[8] K. R. A. Hazzard, B. Gadway, M. Foss-Feig, B. Yan, S. A. Moses, J. P. Covey, N. Y. Yao, M. D. Lukin, J. Ye, D. S. Jin, and A. M. Rey, Phys. Rev. Lett. **113**, 195302 (2014).

[9] A. Frisch, M. Mark, K. Aikawa, S. Baier, R. Grimm, A. Petrov, S. Kotochigova, G. Quéméner, M. Lepers, O. Dulieu, and F. Ferlaino, Phys. Rev. Lett. **115**, 203201 (2015).

[10] F. Seeßelberg, N. Buchheim, Z.-K. Lu, T. Schneider, X.-Y. Luo, E. Tiemann, I. Bloch, and C. Gohle, Phys. Rev. A **97**, 013405 (2018).

[11] M. Lu, N. Q. Burdick, and B. L. Lev, Phys. Rev. Lett. **108**, 215301 (2012).

[12] M. Lu, N. Q. Burdick, S. H. Youn, and B. L. Lev, Phys. Rev. Lett. **107**, 190401 (2011).

[13] B. Capogrosso-Sansone, C. Trefzger, M. Lewenstein, P. Zoller, and G. Pupillo, Phys. Rev. Lett. **104**, 125301 (2010).

[14] T. Sowiński, O. Dutta, P. Hauke, L. Tagliacozzo, and M. Lewenstein, Phys. Rev. Lett. **108**, 115301 (2012).

[15] M. Maik, P. Hauke, O. Dutta, M. Lewenstein, and J. Zakrzewski, New J. Phys. **15**, 113041 (2013).

[16] K. Biedroń, M. Łącki, and J. Zakrzewski, Phys. Rev. B **97**, 245102 (2018).

[17] K. Baumann, C. Guerlin, F. Brennecke, and T. Esslinger, Nature (London) **464**, 1301 (2010).

[18] R. Landig, L. Hruby, N. Dogra, M. Landini, R. Mottl, T. Donner, and T. Esslinger, Nature (London) **532**, 476 (2016).

[19] B. Sundar and E. J. Mueller, Phys. Rev. A **94**, 033631 (2016).

[20] H. Habibian, A. Winter, S. Paganelli, H. Rieger, and G. Morigi, Phys. Rev. Lett. **110**, 075304 (2013).

[21] N. Dogra, F. Brennecke, S. D. Huber, and T. Donner, Phys. Rev. A **94**, 023632 (2016).

[22] T. Flottat, L. de Forges de Parny, F. Hébert, V. G. Rousseau, and G. G. Batrouni, Phys. Rev. B **95**, 144501 (2017).

[23] C. Zhang and H. Rieger, Front. Phys. **7**, 236 (2020).

[24] H. Habibian, A. Winter, S. Paganelli, H. Rieger, and G. Morigi, Phys. Rev. A **88**, 043618 (2013).

[25] C. Zhang and H. Rieger, Eur. Phys. J. B **93**, 25 (2020).

[26] C. Zhang, A. Safavi-Naini, and B. Capogrosso-Sansone, Phys. Rev. A **97**, 013615 (2018).

[27] D. Grimmer, A. Safavi-Naini, B. Capogrosso-Sansone, and S. G. Soyler, Phys. Rev. A **90**, 043635 (2014).

[28] F. Lingua, B. Capogrosso-Sansone, A. Safavi-Naini, A. J. Jahangiri, and V. Penna, Phys. Scr. **93**, 105402 (2018).

[29] A. Safavi-Naini, B. Capogrosso-Sansone, and A. Kuklov, Phys. Rev. A **90**, 043604 (2014).

[30] I. Danshita and C. A. R. Sa de Melo, Phys. Rev. Lett. **103**, 225301 (2009).

[31] H.-K. Wu and W.-L. Tu, Phys. Rev. A **102**, 053306 (2020).

[32] S. Bandyopadhyay, R. Bai, S. Pal, K. Suthar, R. Nath, and D. Angom, Phys. Rev. A **100**, 053623 (2019).

[33] C. Zhang, A. Safavi-Naini, A. M. Rey, and B. Capogrosso-Sansone, New J. Phys. **17**, 123014 (2015).

[34] S. G. Bhongale, L. Mathey, S.-W. Tsai, C. W. Clark, and E. Zhao, Phys. Rev. Lett. **108**, 145301 (2012).

[35] M. M. Parish and F. M. Marchetti, Phys. Rev. Lett. **108**, 145304 (2012).

[36] Y. Yamaguchi, T. Sogo, T. Ito, and T. Miyakawa, Phys. Rev. A **82**, 013643 (2010).

[37] A. Macia, D. Hufnagl, F. Mazzanti, J. Boronat, and R. E. Zillich, Phys. Rev. Lett. **109**, 235307 (2012).

[38] L. M. Sieberer and M. A. Baranov, Phys. Rev. A **84**, 063633 (2011).

[39] K. Sun, C. Wu, and S. Das Sarma, Phys. Rev. B **82**, 075105 (2010).

[40] J. K. Block, N. T. Zinner, and G. M. Bruun, New J. Phys. **14**, 105006 (2012).

[41] N. V. Prokof'ev, B. V. Svistunov, and I. S. Tupitsyn, J. Exp. Theor. Phys. **87**, 310 (1998).

[42] W. Kohn, Phys. Rev. **115**, 809 (1959).

[43] O. Dutta, M. Gajda, P. Hauke, M. Lewenstein, D.-S. Lühmann, B. A. Malomed, T. Sowiński, and J. Zakrzewski, Rep. Prog. Phys. **78**, 066001 (2015).

[44] E. L. Pollock and D. M. Ceperley, Phys. Rev. B **36**, 8343 (1987).

[45] J. Hubbard, Phys. Rev. B **17**, 494 (1978).

[46] M. E. Fisher and W. Selke, Phys. Rev. Lett. **44**, 1502 (1980).

[47] P. Bak and R. Bruinsma, Phys. Rev. Lett. **49**, 249 (1982).

[48] R. Kraus, K. Biedroń, J. Zakrzewski, and G. Morigi, Phys. Rev. B **101**, 174505 (2020).

[49] B. Naylor, A. Reigue, E. Maréchal, O. Gorceix, B. Laburthe-Tolra, and L. Vernac, Phys. Rev. A **91**, 011603(R) (2015).

[50] K. Aikawa, A. Frisch, M. Mark, S. Baier, A. Rietzler, R. Grimm, and F. Ferlaino, Phys. Rev. Lett. **108**, 210401 (2012).

[51] K. Aikawa, A. Frisch, M. Mark, S. Baier, R. Grimm, and F. Ferlaino, Phys. Rev. Lett. **112**, 010404 (2014).

[52] D. Booth, S. T. Rittenhouse, J. Yang, H. R. Sadeghpour, and J. P. Shaffer, Science **348**, 99 (2015).

[53] M. Greiner, O. Mandel, T. Esslinger, T. W. Hänsch, and I. Bloch, Nature (London) **415**, 39 (2002).

[54] I. Bloch, J. Dalibard, and W. Zwerger, Rev. Mod. Phys. **80**, 885 (2008).

[55] J. F. Sherson, C. Weitenberg, M. Endres, M. Cheneau, I. Bloch, and S. Kuhr, Nature (London) **467**, 68 (2010).

[56] J. Simon, W. S. Bakr, R. Ma, M. E. Tai, P. M. Preiss, and M. Greiner, Nature (London) **472**, 307 (2011).

[57] J. Yang, L. Liu, J. Mongkolkiattichai, and P. Schauss, arXiv:2102.11862.

[58] D.-S. Lühmann, O. Jürgensen, and K. Sengstock, New J. Phys. **14**, 033021 (2012).

[59] T. Best, S. Will, U. Schneider, L. Hackermüller, D. van Oosten, I. Bloch, and D. S. Lühmann, Phys. Rev. Lett. **102**, 030408 (2009).